# Supplementary Materials - Deterministic photon source of genuine three-qubit entanglement

Yijian Meng,[1] Ming Lai Chan,[1] Rasmus B. Nielsen,[1] Martin H. Appel,[1,3] Zhe Liu,[1] Ying Wang,[1] Nikolai Bart,[2]
Andreas D. Wieck,[2] Arne Ludwig,[2] Leonardo Midolo,[1] Alexey Tiranov,[1,4] Anders S. Sørensen,[1] and Peter Lodahl[1,*]

[1]*Center for Hybrid Quantum Networks (Hy-Q), The Niels Bohr
Institute, University of Copenhagen, DK-2100 Copenhagen Ø, Denmark*
[2]*Lehrstuhl für Angewandte Festörperphysik, Ruhr-Universität Bochum, Universitätsstraße 150, 44801 Bochum, Germany*
[3]*Present address: Cavendish Laboratory, University of Cambridge, JJ Thomson Avenue, Cambridge, CB30HE, United Kingdom*
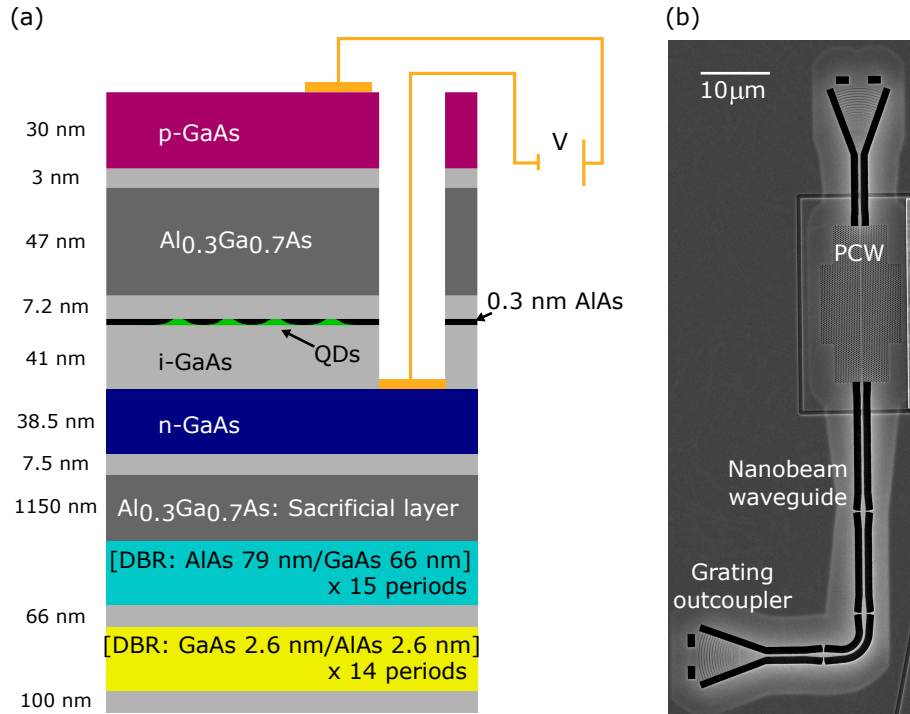[4]*Present address: Chimie ParisTech, Université PSL, CNRS, Institut de Recherche de Chimie Paris, 75005 Paris, France*

## CONTENTS

---

* Corresponding author: lodahl@nbi.ku.dk

# I. COMPOSITION OF THE QUANTUM DOT DEVICE



**Supplementary Figure** 1. (a) Wafer composition of the *p-i-n* diode containing self-assembled InAs quantum dots. A 0.3 nm AlAs layer prevents occupation of the electron wetting layer states [S1]. Applying a bias voltage V across the diode deterministically charges the QD with an electron. (b) Waveguide device used in the experiment. The photonic-crystal waveguide (PCW) uses crystal lattice constant of 246 nm and hole radius of 70 nm in the slow light region.

Our sample is grown by molecular beam epitaxy containing a single layer of self-assembled InAs quantum dots capped by GaAs, embedded in a *p-i-n* diode. A forward DC bias voltage V is applied across the diode to stabilize the charge environment, deterministically charge the QD with an electron and tune the frequencies of QD optical transitions via the quantum-confined DC Stark effect [S2]. Supplementary Fig. 1 outlines the heterostructure of the diode. A 174 nm-thin GaAs membrane spanning from the hole-rich *p*-doped to the electron-rich *n*-doped layers is grown on top of the $Al_{0.3}Ga_{0.7}As$ sacrificial layer. The layer of InAs QDs (green) is located at the center of the membrane for maximal coupling to the optical field. Detailed fabrication steps of the wafer can be found in Ref. [S3]. To fabricate suspended photonic-crystal waveguides (see Supplementary Fig. 1(b)), the sacrificial layer is first removed using hydrofluoric acid followed by nanostructure etching with electron-beam lithography and reactive ion etching [S3, S4]. Underneath the sacrificial layer is an addition of two stacks of distributed Bragg reflectors (DBR), which increases the reflection of downward-scattered light by 60% [S3]. This is different than the DBR-absent wafer used in Ref. [S3], and is shown to improve the grating coupler efficiency from 60% to 80% [S3].

## II.   OPTICAL IMAGING SETUP AND SAMPLE MOUNT
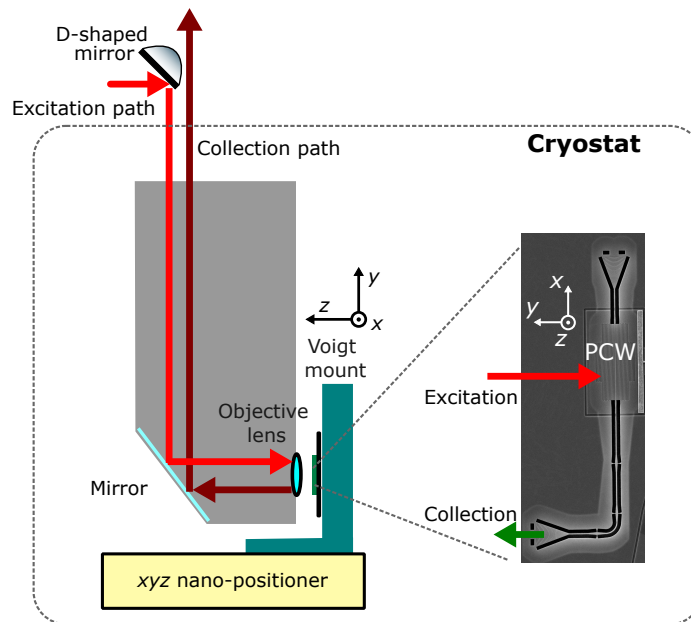


**Supplementary Figure** 2. Optical imaging setup.

The GaAs photonic chip is placed inside a closed-cycle cryostat (attoDRY1000) at $4\,\mathrm{K}$, which contains a vector magnet that generates up to a maximum $5\,\mathrm{T}$ magnetic field along the $y$-direction and $2\,\mathrm{T}$ in $x$ (indicated in Supplementary Fig. 2). To utilize a high magnetic field ($> 2\,\mathrm{T}$) in the Voigt geometry, the chip is mounted on a custom-made L-shape sample mount (dark green) such that the magnetic field is exerted in-plane relative to the waveguide device. The waveguide structure is brought to focus by translating 3 piezo nano-positioners beneath the sample mount.

To increase the photon collection efficiency, we use a D-shaped mirror to reflect the excitation light into the microscope objective, which consists of a single lens with a working distance of 1.61 mm and a numerical aperture of 0.68. Due to $\approx 70\,\mu\mathrm{m}$ spatial separation between QD position and the collection grating coupler in the photonic-crystal waveguide, QD-emitted photons from the coupler are directed towards free space without intercepting on the D-shape mirror and are subsequently collected. Compared to the previous work where a 50:50 beamsplitter was used [S5], the current design improves both the excitation and collection efficiencies by twofold.

# III.   ELECTRONIC SETUP FOR OPTICAL SPIN CONTROL
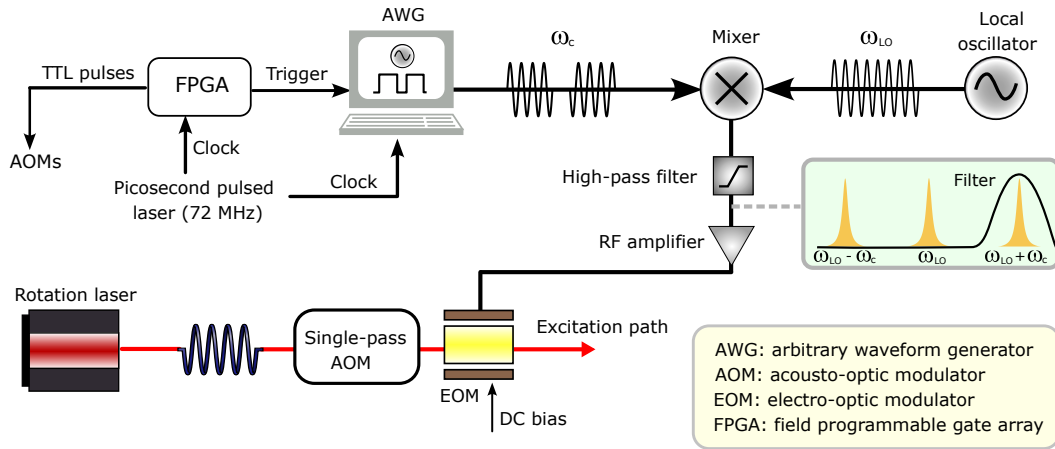


**Supplementary Figure** 3. Illustration of the electron spin rotation setup.

Optical spin control pulses are generated by modulating a laser (CTL from Toptica) with a microwave source. The laser propagates through a single-pass acoustic-optic modulator (AOM) setup, and subsequently through an electro-optic modulator (EOM) to generate bi-chromatic nanosecond optical pulses. The EOM is amplitude-modulated by microwave pulses generated using an arbitrary waveform generator (AWG, Active Technologies AWG5064). Since the AWG carrier frequency $\omega_c$ is limited to a maximum 6 GHz, it is first mixed with another microwave source (local oscillator in Supplementary Fig. 3) of frequency $\omega_{LO}$ using a frequency mixer to match the tens of GHz Zeeman ground-state splitting of the electron spin.

The AWG has an internal IQ mixer which offers flexible control over the relative phase between different pulses. The RF signal out of the AWG is first frequency up-converted via a frequency mixer (Mini-Circuits ZX05-153LH-S+), which creates two frequency sidebands $\omega_{LO} \pm \omega_c$. Next, The low-frequency band is filtered out using a high band-pass filter (Mini-Circuits ZVBP-10R5G-S+), while the high-frequency band is amplified by a broadband amplifier (ixBlue DR-PL-20-MO). The amplified RF signal is then used to amplitude-modulate the optical signal passing through the EOM (ixBlue NIR-MX800-LN-10), resulting in bi-chromatic pulses (i.e., with two optical sidebands) to drive the two-photon Raman transition. In the current work, $\omega_c = 2.8$ GHz and $\omega_{LO} = 8.2$ GHz are set to drive an electron Zeeman ground-state splitting of $\Delta_g = 2(\omega_c + \omega_{LO}) = 22$ GHz at 4 T. The factor of 2 stems from the frequency difference between two sidebands.

To synchronize between the optical excitation pulses, spin readout, cooling and rotation pulses in the entanglement pulse sequence, an external RF clock signal of 72.63 MHz generated by a picosecond Ti:Sapphire laser (Coherent MIRA 900 P) is first divided into two clock signals via a BNC T-splitter to synchronize with the AWG and a custom-made field programmable gate array (Cyclone V FPGA from Intel), respectively. The FPGA outputs TTL signals to produce trigger to the AWG and a time-to-digital converter (Time Tagger Ultra) as well as square pulses for other AOMs (e.g., for spin readout). The photon detection events are recorded using Time Tagger Ultra and superconducting nanowire single-photon detectors with a timing jitter of 260-290 ps.

## IV.   ENTANGLEMENT PULSE SEQUENCE AND EXPERIMENTAL PROCEDURE

In this section, we show explicit steps for generating three-qubit entanglement and elaborate on the experimental procedure used in the experiment. The entanglement sequence for the three-qubit GHZ state can be written in the following:

Step 1: Initialize the electron spin state in $|\uparrow, \emptyset, \emptyset\rangle$ by optical spin pumping.

Step 2: First $\pi/2$ rotation pulse drives the spin to $(|\uparrow, \emptyset, \emptyset\rangle - |\downarrow, \emptyset, \emptyset\rangle)/\sqrt{2}$.

Step 3: Optical excitation with a resonant picosecond pulse produces an early photon conditioned on the spin state $|\downarrow\rangle$: $(|\uparrow, \emptyset, \emptyset\rangle - |\downarrow, e, \emptyset\rangle)/\sqrt{2}$.

Step 4: A $\pi$ rotation pulse flips the spin ground state to $(-|\downarrow, \emptyset, \emptyset\rangle - |\uparrow, e, \emptyset\rangle)/\sqrt{2}$.

Step 5: Another excitation pulse produces a late photon $(-|\downarrow, l, \emptyset\rangle - |\uparrow, e, \emptyset\rangle)/\sqrt{2}$.

Step 6: A $\pi$ rotation pulse flips the spin to $(-|\uparrow, l, \emptyset\rangle + |\downarrow, e, \emptyset\rangle)/\sqrt{2}$.

Step 7: A resonant excitation pulse produces an early photon $(-|\uparrow, l, \emptyset\rangle + |\downarrow, e, e\rangle)/\sqrt{2}$.

Step 8: A $\pi$ rotation pulse flips the spin state to $(|\downarrow, l, \emptyset\rangle + |\uparrow, e, e\rangle)/\sqrt{2}$.

Step 9: A resonant excitation pulse produces a late photon $(|\downarrow, l, l\rangle + |\uparrow, e, e\rangle)/\sqrt{2}$.

Step 10: A $\pi$ rotation pulse flips the spin state to $(|\uparrow, l, l\rangle - |\downarrow, e, e\rangle)/\sqrt{2}$.

Here we use the notation $|\uparrow, \emptyset, \emptyset\rangle$ where the first, second, and third place corresponds to the state of the spin, first photon and second photon, respectively. $|\emptyset\rangle$ denotes the vacuum state. Note that steps 7 to 10 are a repetition of steps 3 to 6. If steps 6 and 10 are each replaced with $\pi/2$ pulse, the final state corresponds to a three-qubit cluster state.

Supplementary Fig. 4 shows the time-resolved histogram of the GHZ measurement sequence. The first (second) three peaks correspond to the detection of the first (second) photonic qubit using the self-stabilized time-bin interferometer. Shaded bars indicate the time gating used for acquiring photon clicks, which we set to be 1 ns and 100 ns for the photonic and spin qubits, respectively.

To reduce the effect of power drift of the rotation laser at the quantum dot, i.e., pointing instability, we perform interleaving sequences of three-qubit measurement and spin Rabi oscillation. We calculate a scaling ratio between the desired spin Rabi frequency $\Omega_r^i$ for a 4 ns $\pi$-pulse and Rabi frequency $\Omega_r^f$ fitted from the spin Rabi oscillation. We then adjust the power of the rotation laser in the subsequent iteration by multiplying it by a factor of $\Omega_r^i/\Omega_r^f$. Note that the rotation laser power $P_{\text{rot}} \propto \Omega_r$ since the spin rotation is a two-photon process.
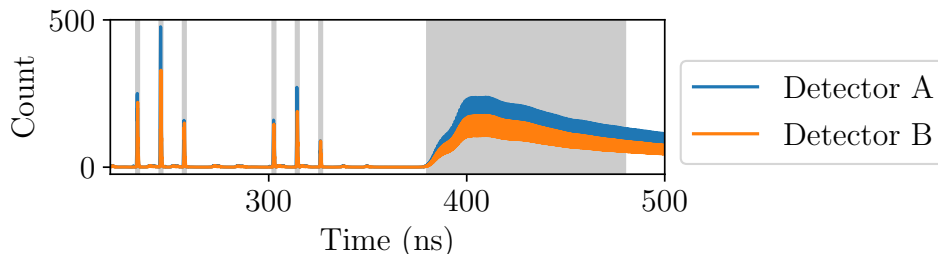


**Supplementary Figure** 4.   Histogram of the experimental sequence in the first 500 ns. The blue and yellow curves correspond to the measurements on the two detectors, respectively. The first (second) three pulses corresponds to the first (second) photonic qubit whereas the last long shaded area corresponds to the spin qubit. The rotation pulses (-650 GHz) are filtered out before the detectors using a pair of Etalon filters (3 GHz FWHM).
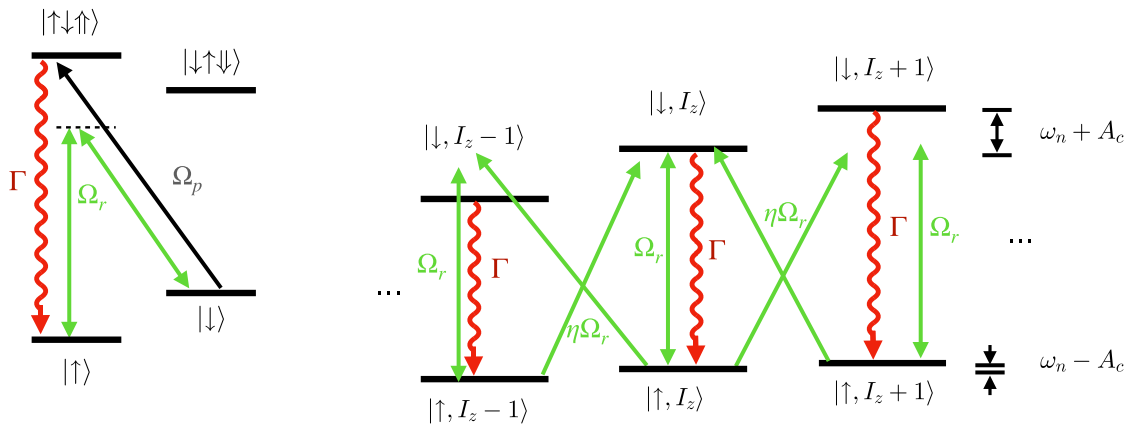
**Supplementary Figure** 5. Schematic diagram for nuclear spin cooling. Due to Overhauser shift, the electron spin resonance(ESR) depends on the net nuclear spin polarization $I_z$.

## V. NUCLEAR SPIN NARROWING

In this section, we explain the mechanism of nuclear spin narrowing process that was also detailed in the literature [S6]. Supplementary Fig. 5 shows the level diagram of a electron spin coupled to the nearby nuclear spin ensemble. The nuclear spin narrowing process is analogous to Raman cooling in cold atom: The Raman laser induces energy exchange between the net nuclear spin polarization $I_z$ and the spin, while another pump laser dissipates the energy of the spin degree of freedom, increasing (decreasing) of $I_z$ when the Raman frequency $\omega_r$ is red(blue) detuned from the electron spin resonance(ESR) $\omega_{\mathrm{ESR}}$.

The mechanism for nuclear spin narrowing can be further explained in Fig. 5. Here the Raman frequency is resonant to ESR at $I_z$ and the spin dissipates from $|\downarrow\rangle$ to $|\uparrow\rangle$ at a rate of $\Gamma$. The ESR is shifted by the Overhauser interaction by $2A_c I_z$, where $A_c$ is the hyperfine coupling energy per nucleus. When the net nuclear spin polarization reduces to $I_z - 1$, the net polarization increasing transitions such as $|\uparrow, I_z - 1\rangle \rightarrow |\downarrow, I_z\rangle$ become closer to resonant compared to the decreasing transitions such as $|\uparrow, I_z\rangle \rightarrow |\downarrow, I_z - 1\rangle$ or $|\uparrow, I_z - 1\rangle \rightarrow |\downarrow, I_z - 2\rangle$. After further dissipation from $|\downarrow\rangle$ to $|\uparrow\rangle$, the net polarization increases after this process. Similarly, when the net nuclear spin polarization increases above $I_z$, the net polarization decreasing transitions are more resonant and thus in combination with the dissipation channel, the net polarization is reduced.

During nuclear spin narrowing, the ESR corresponding to $I_z$ becomes a stable point and the frequency fluctuation around $I_z$ is reduced. Therefore, the measured Ramsey time is significantly increased due to the stabilized ESR.

## VI. OPTICAL CYCLICITY MEASUREMENT

To estimate optical cyclicity of the negatively charged QD in a PCW, we follow the approach in Ref. [S7] to perform two sets of measurements shown in Supplementary Fig. 6. For the first measurement, we measure its radiative lifetime using $p$-shell excitation by a picosecond Ti:Sapphire laser (Coherent MIRA 900P) locked at $\approx 20\,\mathrm{nm}$ blue-detuned from the QD resonance. We fit the radiative decay with a single exponential function and extract a lifetime of $1/\Gamma = 235(1)$ ps, suggesting a waveguide-induced Purcell enhancement of 4.2 compared to $\tau_o \approx 1\,\mathrm{ns}$ in bulk.

The decay rate $\gamma_Y$ of the inhibited optical transition $|\uparrow\downarrow\Uparrow\rangle \rightarrow |\uparrow\rangle$ can then be estimated from fitting its optical pumping rate $\gamma_{\mathrm{osp}}$ as a function of probe power $P$. We perform two-color spin pumping measurements, where a 400 ns probe pulse drives the transition $|\downarrow\rangle \rightarrow |\uparrow\downarrow\Uparrow\rangle$ with optical Rabi frequency $\Omega_p = \Gamma\sqrt{P/P_{\mathrm{sat}}}$ controlled by $P$ and saturation power $P_{\mathrm{sat}}$. At each power, we fit the fluorescence decay during the probe pulse with a single exponential to extract $\gamma_{\mathrm{osp}}$. From here a list of values of $\gamma_{\mathrm{osp}}$ as a function of $P$ is obtained (Supplementary Fig. 6(b)) and subsequently fitted with the function [S7]:

$$\gamma_{\mathrm{osp}}(P) = \gamma_Y \int G(\delta_e, \sigma_e) \frac{P/P_{\mathrm{sat}}}{2P/P_{\mathrm{sat}} + 1 + 4\delta_e^2/\Gamma^2} d\delta_e, \tag{1}$$

where $\delta_e$ is the laser detuning from resonance, $G(\delta_e, \sigma_e)$ is a Gaussian distribution of spectral diffusion with a standard
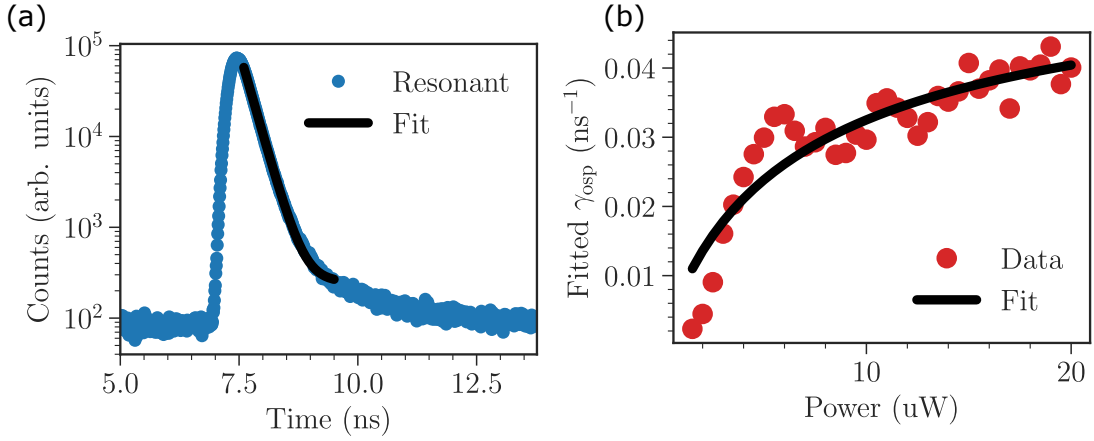
**Supplementary Figure** 6. (a) Time-resolved fluorescence decay of a negatively charged QD measured at 0 T magnetic field at bias voltage 1.331 V. The QD lifetime is extracted from a single exponential fit. (b) Rate of optical pumping as a function of the pump power.

deviation in drift of $\sigma_e = 2\pi \cdot 0.532$ GHz (extracted independently from the spectral broadening observed in resonant fluorescence spectroscopy). The fit results in $\gamma_Y = 0.114(9)$ ns$^{-1}$ yielding an optical cyclicity of

$$C \equiv \frac{\gamma_X}{\gamma_Y} = \frac{\Gamma - \gamma_Y}{\gamma_Y} = 36(3), \tag{2}$$

which is 2.5 times larger than that of the previous QD reported in Ref. [S7].

## VII. EXPERIMENTAL VERIFICATION OF TWO-QUBIT ENTANGLEMENT

As a complementary measurement, we also generate a two-qubit entangled Bell state consisting of an electron spin and a single photon and measure its fidelity. The entangled state is generated by implementing a single repetition of the protocol depicted in Fig. 2a of the main text. Note that the $\pi$-rotation pulse applied after emission of the late time-bin is used only for spin projection in the $-z$-basis. For characterizing spin-photon correlations in the equatorial basis, this rotation pulse is therefore replaced by a $\pi/2$-pulse to form a spin-echo sequence, as has been previously done in Ref. [S5].

The spin-photon entanglement fidelity is exactly decomposed into $\mathcal{F}_{\text{Bell}} = \text{Tr}\{\rho_{\text{exp}}|\psi_{\text{Bell}}\rangle\langle\psi_{\text{Bell}}|\} = \text{Tr}\{\rho_{\text{exp}}(\hat{\mathcal{P}}_z + \hat{\chi})/2\}$ [S5], where the ideal spin-photon Bell state is $|\psi_{\text{Bell}}\rangle = \frac{1}{\sqrt{2}}(|e\downarrow\rangle - |l\uparrow\rangle)$. $\hat{\chi} = \frac{1}{2}\sum_k(-1)^k\hat{\mathcal{M}}_k = -\hat{\mathcal{M}}_y + \hat{\mathcal{M}}_x$, $\hat{\mathcal{M}}_x = \hat{\sigma}_x$ and $\hat{\mathcal{M}}_y = -\hat{\sigma}_y$. $\hat{\mathcal{P}}_z = |0\rangle\langle0|^{\otimes 2} + |1\rangle\langle1|^{\otimes 2}$ measures correlations in the $z$-basis. Conditioned on two-photon coincidences between the photon emission window and spin readout, the probabilities of measuring the spin-photon state in different bases are reported in Supplementary Fig. 7, with the corresponding expectation values documented in Supplementary Table 1. The measured fidelity exceeds the classical bound of 50% by 52 standard deviations, demonstrating two-qubit entanglement.
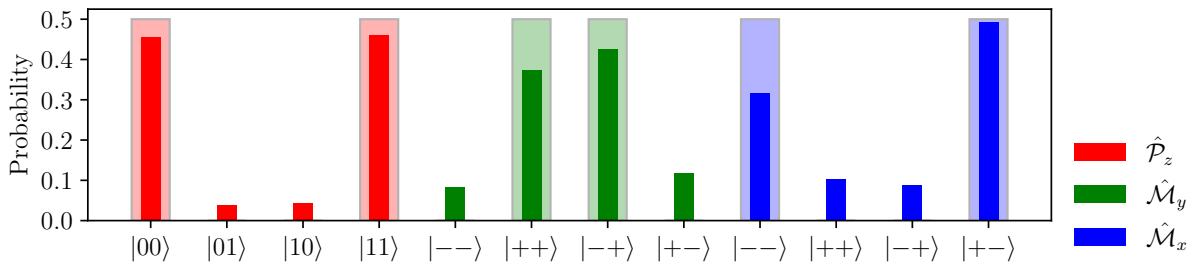


**Supplementary Figure** 7. Fidelity characterization of two-qubit entanglement. Shaded bars correspond to the ideal case.

| Measurement | Values |
|:-----------:|:-------|
| $\langle \hat{\mathcal{P}}_z \rangle$ | 91.7(4)% |
| $\langle \hat{\mathcal{M}}_y \rangle$ | $-60(1)$% |
| $\langle \hat{\mathcal{M}}_x \rangle$ | 62(1)% |
| $\langle \hat{\chi} \rangle$ | 61(1)% |
| $\mathcal{F}_{\mathrm{Bell}}$ | 76.3(5)% |

**Supplementary Table** 1. Summary of expectation values and fidelity for two-qubit entanglement.

## VIII.   MONTE CARLO SIMULATION

In order to investigate the contributions of various error sources to the state fidelity, we run Monte Carlo simulations taking into account all known errors in the experimental setup. To estimate the future scaling of the entanglement source, we also simulate the fidelity using optimized setups with InAs and GaAs QDs. We verify the validity of the MC simulation by comparing it with analytical expressions derived in Sec. IX.

### A.   Simulation Settings and Summary of Results

Three sets of parameters used for simulations are listed in Supplementary Table 2, corresponding to parameters for the InAs QD in the current experiment, the next iteration with optimized settings (e.g., 90°-rotated waveguide orientation with $\Delta = 30\,\mathrm{GHz}$), and future experiments with GaAs QDs.

| Parameters | Simulation Setup | | |
|:----------:|:----------------:|:-----------:|:--------:|
| | InAs QDs (current) | InAs QDs (optimized) | GaAs QDs |
| Radiative lifetime $1/\Gamma$ | 235 ps | 235 ps | 235 ps |
| Cyclicity $C$ | 36 | 36 | 36 |
| Spin rotation Q-factor Q | 34 | 36 | 68 |
| Spin readout fidelity $F_{\mathrm{r}}$ | 98% | 99% | 99% |
| Spin initialization fidelity $F_{\mathrm{int}}$ | 99% | 99% | 99% |
| Pure dephasing rate $\gamma_d$ | 0.069 ns$^{-1}$ | 0.069 ns$^{-1}$ | 0.069 ns$^{-1}$ |
| Excitation laser detuning | $-2\,\mathrm{GHz}$ | 0 GHz | 0 GHz |
| Frequency splitting between cycling transitions $\Delta$ | 10 GHz | 30 GHz | 30 GHz |
| Excitation pulse shape | Gaussian | Gaussian | Gaussian |
| Excitation pulse area | $0.7\pi$ | $1\pi$ | $1\pi$ |
| Excitation pulse duration (FWHM intensity) | 30 ps | 30 ps | 30 ps |
| High-frequency nuclear spin noise | ✓ | ✓ | ✗ |

**Supplementary Table** 2. List of parameters used for the simulation. The excitation laser detuning is the detuning of the excitation laser relative to the targeted cycling transition. The amplitude of nuclear spin noise is extracted from the spin echo visibility measurement, see Sec. VIII B. For simulations in GaAs QDs, we assume the nuclear spin noise to be negligible.

In the optimized setup, the increased frequency splitting $\Delta = 30\,\mathrm{GHz}$ due to the rotated waveguide implies that we can use a full $\pi$-pulse for resonant optical excitations, as the probability of off-resonant excitation becomes negligible with a larger $\Delta$. We also expect a modest improvement of the spin readout fidelity to 99%, owing to the larger $\Delta$. For the simulation with GaAs QDs, we take $\Delta = 30\,\mathrm{GHz}$ and assume that the spin rotation Q-factor can be improved by a factor of two with negligible nuclear spin noise. In all cases, we take the pure dephasing rate $\gamma_d \approx 0.069\,\mathrm{ns}^{-1}$ using the formula $V_s \equiv \Gamma/(\Gamma + 2\gamma_d)$ [S8] where $V_s = 96.8\%$ is the single-photon indistinguishability extracted in Fig. 4d of the main text.

To investigate the contribution of experimental imperfections to the state fidelity, we run Monte Carlo simulations using each set of error parameters in Supplementary Table 2. The simulated results for the current experiment are summarized in Supplementary Table 3. To isolate the contribution of individual error sources, we first run simulations taking into account all errors, which yields an entanglement fidelity $\mathcal{F}_o$. We then perform a second simulation to extract the fidelity $\mathcal{F}_p$ where an error source $p$ is removed from the simulation. The fidelity error due to $p$ alone can therefore be estimated as $\mathcal{F}_p - \mathcal{F}_0$. Although this approach assumes that all errors are independent, it gives a useful estimate of

what to focus on for further optimization. Apart from three main fidelity error contributions mentioned in Table 1 of the main text, here in Supplementary Table 3 the corresponding fidelity error from imperfect spin readout, phonon-induced pure dephasing of the excited state and finite optical cyclicity are also included. Note that the simulated fidelity obtained is averaged over $10^4$ Monte Carlo simulations.

| All error sources | Fidelity error |
|---|---|
| Off-resonant excitation | 11.4 % |
| Nuclear spin noise | 6.0 % |
| Spin-flip error during rotation | 3.2 % |
| Spin readout error | 1.2 % |
| Phonon-induced pure dephasing | 0.7 % |
| Finite cyclicity | 0.6 % |

**Supplementary Table** 3. Simulated fidelity error contribution. The error contribution due to a source $p$ is calculated as the difference in simulated fidelity with and without $p$.

## B. Simulation of Nuclear Spin Noise for Spin-echo Visibility Measurement
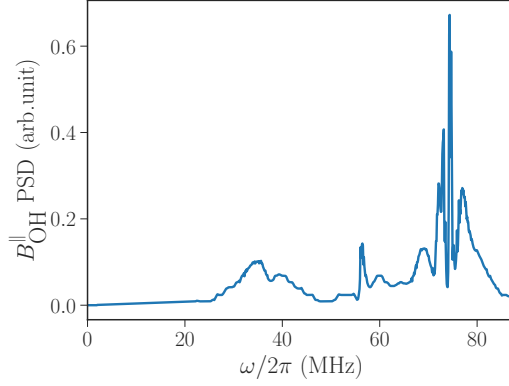


**Supplementary Figure** 8. Power spectral density (PSD) of the linearly coupled Overhauser field component along the quantization direction of the electron spin. Here $\omega$ is the frequency of the noise arising from the Larmor precession of nuclear spins. This plot is reproduced from Stockhill, et al., (2016) [S9].

To simulate the effect of high-frequency nuclear spin noise in InAs QD on the spin-echo visibility measurement (Fig. 3c of the main text), we first obtain the nuclear noise spectrum by reconstructing the power spectral density (PSD) of the linearly coupled Overhauser field component $B_{\mathrm{OH}}^{\parallel}$ (the superscript "$\parallel$" denotes field projection along the quantization direction of the electron spin) originating from In, Ga and As nuclear spins using the data provided in Ref. [S9]. Due to the interplay between Larmor precession of different nuclei species, the linearly coupled Overhauser field noise $\delta B_{\mathrm{OH}}^{\parallel}$ acting on the electron spin also oscillates according to the PSD, resulting in collapse and revival of the spin echo signal. Supplementary Fig. 8 shows the relative amplitude between different nuclear noise frequency components. To simulate the spin echo visibility corresponding to the PSD noise spectrum, we express the phase $\Phi$ induced on the electron spin superposition state $|\uparrow\rangle + e^{i\Phi}|\downarrow\rangle$ in terms of the discretized PSD with a 1 MHz resolution:

$$\Phi_j = A \sum_i \sqrt{\mathrm{PSD}(\omega_i)} \int_{t_j}^{t_{j+1}} \sin(\omega_i t + \phi_i) dt, \tag{3}$$

where the square root of the power spectrum $\sqrt{\mathrm{PSD}(w_i)}$ is used to weigh each frequency component $w_i$, and we assign each $w_i$ a random phase $\phi_i$ at the beginning of the simulation. Here the phase $\Phi_j$ is accumulated over the waiting time between $\pi/2$- or $\pi$-rotation pulses, i.e., in a spin echo sequence, where the subscript $j = 1$ ($j = 2$) is the phase accumulated between the first (second) $\pi/2$ pulse at time $t_1$ ($t_3$) and the middle $\pi$-pulse at time $t_2$. We multiply all frequency components with a common amplitude $A$ which is the only fitting parameter. The visibility in the spin echo sequence is measured by the classical contrast in spin readout counts between two opposite phases of the last $\pi/2$-rotation pulse, which corresponds to $|\cos(\Phi_2 - \Phi_1) + 1|/2$. The zero-frequency component of $\delta B_{\mathrm{OH}}^{\parallel}$ (which determines the spin dephasing time $T_2^*$) is assumed to be filtered out by the spin echo sequence.

To fit the experimental spin echo data in the main text, we fix the visibility at the zero echo delay to 90%, limited by 98% $\pi$-rotation fidelity and 2% spin initialization error. The obtained fit exhibits strong agreement with the experimental data, specifically demonstrating a rapid decay and subsequent revival of echo visibility as the spin echo spacing increases (see main text Fig. 3).

# IX. COMPARISON OF MONTE CARLO SIMULATION WITH THEORY

To further validate our simulated results, we now compare the simulated three-qubit fidelity with analytical fidelity expressions for various error sources. For investigating scalability of the time-bin protocol towards more entangled photons, the analytical theory enables generalization of the entanglement fidelity to $N$ photons. The fidelity error per generated photon can also be obtained from the fidelity slope, which is useful for computing the error thresholds of quantum computing architectures. Note that $N = n - 1$, where $n$ is the total number of qubit including the QD spin.

## A. Optical Cyclicity

The GHZ entanglement protocol relies on repeated optical excitations of the same transition to emit single photons of identical frequency and polarization into each time-bin. This requires an optical transition with a strong preferential decay channel which preserves the spin state, and is quantified by the ratio between dominant and inhibited decay rates $C \equiv \gamma_X / \gamma_Y > 1$. The effect of finite cyclicity $C$ on the $N$-photon GHZ fidelity has been theoretically investigated in Ref. [S10], where the fidelity was perturbatively expanded to first order:

$$\mathcal{F}_{\mathrm{GHZ}}^{(N)} \approx 1 - \frac{1}{2(C+1)}\left(N - \frac{1}{2}\right),\tag{4}$$

which holds when frequency filtering is applied. For estimation of the GHZ state fidelity, the cyclicity error is simulated by introducing a probability of Raman spin-flip process $1/(1+C)$ during optical excitations, where the spin can be flipped by the operator $|\uparrow\rangle\langle\downarrow|$.

Supplementary Fig. 9(a) plots the simulated three-qubit fidelity $\mathcal{F}_{\mathrm{GHZ}}^{(2)}$ as a function of cyclicity $C$, which agrees well with Eq. (4). In Supplementary Fig. 9(b) we also plot $\mathcal{F}_{\mathrm{GHZ}}^{(N)}$ versus photon number $N$, at different values of $C$. Black circles correspond to fidelities at the current value of cyclicity $C = 36$. A two times improvement in $C$ gives 0.68% fidelity error per photon.
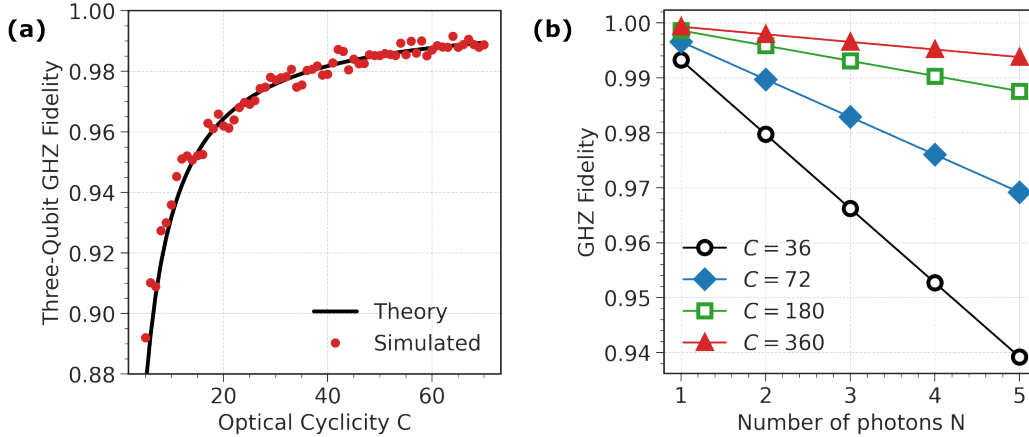


**Supplementary Figure** 9. (a) Comparison between the simulated and analytical fidelities under finite cyclicity $C$. (b) Plot of $\mathcal{F}_{\mathrm{GHZ}}^{(N)}$ as a function of photon number $N$ at different values of $C$.

## B. Incoherent Spin-flip Error

Spin decoherence induced by the spin rotation laser results in depolarization of the entangled spin-photon state, which has previously been observed in Refs. [S5, S11]. Although the decoherence mechanism is not well-understood, here we model the laser-induced spin decoherence as a $T_1$ process, i.e., the QD electron spin is removed by the red-detuned rotation laser [S12] and the QD is later repopulated with a random electron spin state. In our model we assume this process occurs instantaneously. In reality, no photon is detected if the QD spin is absent. It thus has less influence on the fidelity measurement if the process is not instantaneous. This could lead to overestimation of the spin-flip error. After the QD is repopulated, the resulting spin state is assumed to have an equal probability to end up in either $|\uparrow\rangle$ or $|\downarrow\rangle$, which is a reasonable approximation given $\hbar\Delta_g \ll k_B T$, where $\Delta_g$ is ground-state splitting, $T$ is the sample temperature, and $\hbar$ and $k_B$ are the reduced Planck constant and Boltzmann constant, respectively.
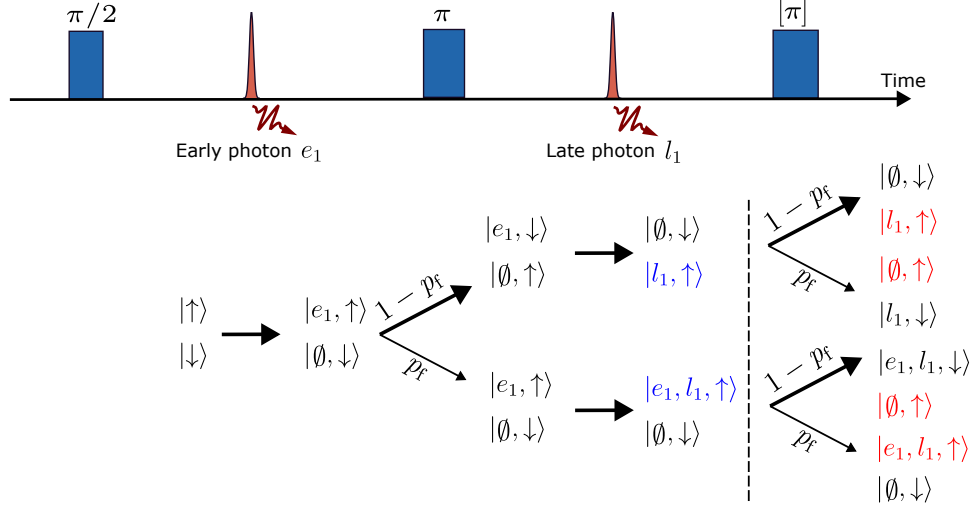


**Supplementary Figure** 10. Estimation of $\langle\hat{\mathcal{P}}_z\rangle$ for 2-qubit state using a tree diagram. After each $\pi$-pulse, there are two possible outcomes with probability of spin-flip ($p_f$, effective $2\pi$ rotation due to the spin flip and $\pi$-pulse) and no spin-flip ($1 - p_f$, effective $\pi$-rotation), respectively. The red (blue) colored states are detected using measurement sequences with (without) the last $\pi$ pulse [$\pi$].

To estimate how spin-flip error affects the entanglement fidelity, we analyze all possible spin-flip events after an entanglement sequence and track down the probabilities of individual states after each operation. During each spin $\pi$-rotation, the spin state has a probability of $p_f = \frac{1}{2}(1 - e^{-\kappa T_\pi})$ to flip its state (on top of the $\pi$ rotation).

As an example, we break down all possible outcomes from the two-qubit entanglement sequence which is shown in a tree diagram (see Supplementary Fig. 10). After the first $\pi/2$-rotation pulse, the resulting state has equal population in $|\uparrow\rangle$ and $|\downarrow\rangle$, regardless of whether a spin flip occurs. Since $\langle\hat{\mathcal{P}}_z\rangle$ evaluates the population contrast between basis states (no coherence terms required), a spin flip during the first $\pi/2$-pulse does not affect the $\langle\hat{\mathcal{P}}_z\rangle$ measurement. However, during the first $\pi$ rotation: If a spin flip occurs, either no photon is emitted ($|\emptyset,\downarrow\rangle$) or both an early photon and a late photon are emitted ($|e_1, l_1, \uparrow\rangle$). The former state does not count toward the overall statistics since no photon is detected, while the latter has twice the probability since photons from both $|e_1, \uparrow\rangle$ and $|l_1, \uparrow\rangle$ can be detected (our collection efficiency is limited, making it unlikely that we detect both). Furthermore, since only $|\uparrow\rangle$ can be measured by optical spin pumping, an additional $\pi$ pulse is used to transfer $|\downarrow\rangle$ to $|\uparrow\rangle$, which leads to 4 additional possible outcomes. Summing over the probability of all detected states, the Z-basis expectation value is:

$$\langle\hat{\mathcal{P}}_z^{(2)}\rangle = \frac{p_f + (1 - p_f) + p_f^2 + (1 - p_f)^2}{2p_f + (1 - p_f) + 2p_f^2 + (1 - p_f)^2} \approx 1 - p_f, \tag{5}$$

where the first-order expansion in the last step further approximates the results to one spin-flip event per entanglement sequence.

Similarly, the $n$-qubit Z-basis expectation value can be expanded in the first order as

$$\langle\hat{\mathcal{P}}_z^{(n)}\rangle \approx 1 - (2n - 3)p_f, \tag{6}$$

For $\langle \hat{\chi} \rangle$, when a spin-flip event occurs, the spin coherence drops to zero as the entangled state becomes mixed. Therefore,

$$\langle \hat{\chi} \rangle = 1 \times (e^{-\kappa T_s}) + 0 \times (1 - e^{-\kappa T_s}) = e^{-\kappa T_s}, \tag{7}$$

where $T_s$ is the total duration of the rotation pulse in a sequence, i.e., $T_s = (2n - 3)T_\pi$.

To validate our Monte Carlo simulation, we compare the above model with the simulated fidelity in Supplementary Fig. 11, which shows good agreement in the limit of $\kappa/\Omega_r \ll 1$. The spin-flip error $\kappa/\Omega_r$ introduces damping to the visibility of Rabi oscillations and is related to the quality factor Q via the $\pi$-pulse duration $T_\pi = \pi/\Omega_r$:

$$\frac{1}{Q} \equiv \frac{T_\pi}{T_{1/e}} = \pi \frac{\kappa}{\Omega_r}, \tag{8}$$

which holds when the rotation fidelity error due to finite $T_2^*$ is negligible, i.e., $\Omega_r \gg 1/T_2^*$. As a subject of interest, in Supplementary Fig. 11(b), $\mathcal{F}_{\text{GHZ}}^{(N)}$ is plotted in the limit of small photon number $N \leq 5$ at various values of Q. Here we observe that a twofold reduction in $\kappa$ (or improvement in Q) could minimize the fidelity error per photon to 2%.
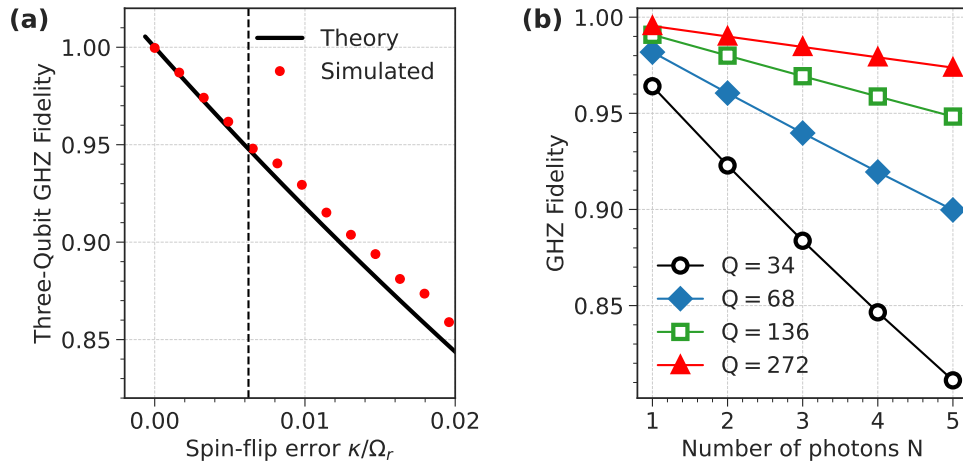


**Supplementary Figure** 11. (a) Comparison between the simulated and analytical fidelities as a function of normalized spin-flip rate $\kappa/\Omega_r$. The vertical dashed line corresponding Q = 34. (b) Plot of $\mathcal{F}_{\text{GHZ}}^{(N)}$ as a function of photon number $N$ for different quality factor Q.
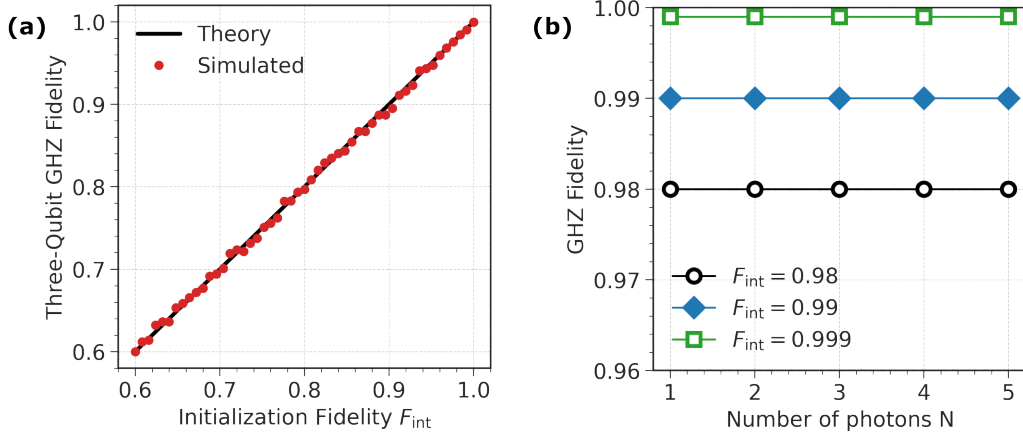
## C. Initialization Fidelity

To account for initialization error in the simulation, we define $F_{int}$ as the probability of successful initialization of the spin state $|\uparrow\rangle$ by optical pumping of the transition $|\downarrow\rangle \rightarrow |\Downarrow\downarrow\uparrow\rangle$. A random number $i \in [0, 1]$ is drawn and compared with $F_{int}$. If $i \leq F_{int}$ ($i > F_{int}$), the initial state becomes $|\uparrow\rangle$ ($|\downarrow\rangle$). Similarly, this error is included in the theory by modifying the spin density matrix $\tilde{\rho}_s$ as

$$\tilde{\rho}_s \rightarrow F_{int}\tilde{\rho}_s + (1 - F_{int})\rho_s^{ideal}, \tag{9}$$

where $\rho_s^{ideal}$ is the spin density matrix after applying a perfect $\pi/2$ pulse on the spin state $|\downarrow\rangle$. It is straightforward to show that the entanglement fidelity is expressed by

$$\mathcal{F}_{GHZ}^{(N)} = F_{int}, \tag{10}$$

which does not depend on the photon number in the generated state. Supplementary Fig. 12(a) compares the simulation and theory, and Supplementary Fig. 12(b) shows that the initialization error is directly mapped to $\mathcal{F}_{GHZ}^{(N)}$ as predicted by Eq. (10).



**Supplementary Figure** 12. (a) Comparison between the simulated and analytical fidelities under initialization error. (b) Plot of $\mathcal{F}_{GHZ}^{(N)}$ as a function of photon number $N$ at different values of $F_{int}$.

## D.  Spin Readout Fidelity

Spin readout is performed in the experiment by optically pumping the $|\downarrow\rangle \rightarrow |\uparrow\downarrow\uparrow\rangle$ transition, where $|\downarrow\rangle$ ($|\uparrow\rangle$) is translated to $|1\rangle$ ($|0\rangle$). To incorporate spin readout error into the simulation, we introduce $F_{\rm r}$ as the fidelity of reading out $|1\rangle$, whereas $1 - F_{\rm r}$ corresponds to the probability of erroneously reading $|0\rangle$. The entanglement fidelity is:

$$\mathcal{F}_{\rm GHZ}^{(N)} = \frac{1}{2}(\langle\hat{\mathcal{P}}_z\rangle + \langle\hat{\chi}\rangle), \tag{11}$$

where

$$\langle\hat{\mathcal{P}}_z\rangle = |0\rangle\langle 0|^{\otimes n} + |1\rangle\langle 1|^{\otimes n}, \qquad \langle\hat{\chi}\rangle = |0\rangle\langle 1|^{\otimes n} + |1\rangle\langle 0|^{\otimes n} = \frac{1}{n}\sum_{k=1}^{n}(-1)^k\langle\hat{\mathcal{M}}_k\rangle. \tag{12}$$

For $\langle\hat{\mathcal{P}}_z\rangle$, reading out the wrong spin results in the detection of the wrong state, i.e, $|1\rangle^{\otimes N}|0\rangle_s\langle 1|^{\otimes N}\langle 0|_s$ or $|0\rangle^{\otimes N}|1\rangle_s\langle 0|^{\otimes N}\langle 1|_s$. Therefore, $\langle\hat{\mathcal{P}}_z\rangle = F_{\rm r} + 0(1 - F_{\rm r}) = F_{\rm r}$.

On the other hand, the measurement of $\langle\hat{\chi}\rangle$ requires projection of each qubit onto $\hat{\mathcal{M}}_k$ basis with eigenstates $|\pm_k\rangle = (|0\rangle \pm e^{ik\pi/n}|1\rangle)/\sqrt{2}$, where $k \leq n$ is the number of qubits. Since in the experiement spin readout is only available in $|1\rangle$, we use two separate measurement configurations for every $\hat{\mathcal{M}}_k$ basis: In one configuration, a spin rotation pulse $\hat{R}(\pi/2, \theta = ik\pi/n)$ is applied to transfer $|+_k\rangle$ ($|-_k\rangle$) to $|1\rangle$ ($|0\rangle$). In the other configuration, $\hat{R}(\pi/2, \theta = ik\pi/n + \pi)$ transfers $|+_k\rangle$ ($|-_k\rangle$) to $|0\rangle$ ($|1\rangle$). Thus, readout of the wrong spin state is equivalent to switching between the $|+\rangle$ and $|-\rangle$ spin states. To see this, $\langle\hat{\chi}\rangle$ can be written as:

$$\langle\hat{\chi}\rangle = |0\rangle\langle 1|^{\otimes n} + |1\rangle\langle 0|^{\otimes n} = \frac{(-1)^k}{2^n}\left[\left((|+_k\rangle - |-_k\rangle)(\langle +_k| + \langle -_k|)\right)^{\otimes n} + \left((|+_k\rangle + |-_k\rangle)(\langle +_k| - \langle -_k|)\right)^{\otimes n}\right]. \tag{13}$$

After factoring out Eq. (13), only the diagonal terms have non-zero coefficients of either $1/2^n$ or $-1/2^n$, depending on the parity of the sum of $k$ and the number of $|-_k\rangle$ terms in the state, i.e., for the two-qubit case, $|+_k+_k\rangle\langle +_k+_k|$ and $|+_k-_k\rangle\langle +_k-_k|$ have opposite signs due to their even and odd numbers of $|-_k\rangle$ terms, respectively. Therefore, $\langle\hat{\chi}\rangle$ is given by the difference between even parity and odd parity terms. By measuring the wrong spin state, i.e., switching between $|+\rangle$ and $|-\rangle$ for the spin qubit, the parity of all diagonal terms is switched with probability $F_{\rm r}$, leading to $\langle\hat{\chi}\rangle = \mathcal{F}_{\rm r} + (-1)(1 - \mathcal{F}_{\rm r})$. The overall readout fidelity is then:

$$\mathcal{F}_{\rm GHZ}^{(N)} = \frac{3\mathcal{F}_{\rm r} - 1}{2}, \tag{14}$$

which is indeed independent of the photon number $N$ in the GHZ state, as spin readout error is always performed at the end of the experimental protocol. In the simulation, the output density matrix is simulated for each measurement setting, and the readout error is introduced as the final step of the simulation. Supplementary Fig. 13 shows great
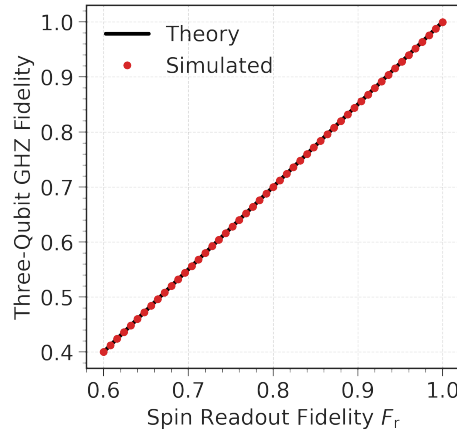


**Supplementary Figure** 13. Comparison between the simulated and analytical fidelities under spin readout error.

agreement between simulated fidelity and the analytical form in Eq. (14).

### E. Phonon-induced Pure Dephasing

Unwanted coupling of the QD optical transition to a phonon thermal bath results in broadening of the QD zero-phonon line as well as a broad phonon sideband [S8, S13–S15]. The former gives rise to dephasing of the excited state at a rate of $\gamma_d$ and subsequenct emission of incoherent photons, which degrade their interference, whereas the latter is filtered out with frequency filters. The effect of phonon-induced pure dephasing on the GHZ fidelity can be expressed by [S10]

$$\mathcal{F}_{\mathrm{GHZ}}^{(N)} = \frac{1}{2} + \frac{1}{2}\left(\frac{\Gamma}{\Gamma + 2\gamma_d}\right)^N, \tag{15}$$

where $\Gamma$ is the total decay rate of the excited state $|\Uparrow\downarrow\uparrow\rangle$. To consider this in the Monte Carlo simulation, we introduce a random phase (0 to $2\pi$) between $|\uparrow\rangle$ and $|\downarrow\rangle$ after each photon generation event, with a probability determined by $\gamma_d/\Gamma$.
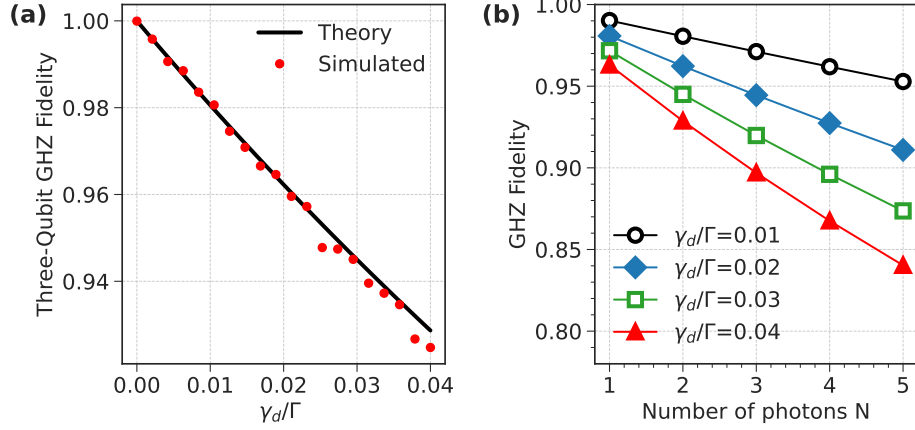


**Supplementary Figure** 14. (a) Comparison between simulated and analytical fidelities under phonon-induced pure dephasing. (b) Plot of $\mathcal{F}_{\mathrm{GHZ}}^{(N)}$ as a function of photon number $N$ for different values of the ratio between $\gamma_d$ and $\Gamma$.

## F. Optical Excitation Errors

In this section, we consider two error mechanisms that occur during optical pulsed excitation of the transition $|\downarrow\rangle \leftrightarrow |\Uparrow\downarrow\uparrow\rangle$. The first error originates from the spectral overlap between the excitation laser and the undesired transition $|\uparrow\rangle \leftrightarrow |\Downarrow\downarrow\uparrow\rangle$, which leads to a non-zero probability of exciting $|\uparrow\rangle$, emitting photons of a different frequency. Although these photons can be filtered out, they lead to dephasing of the coherence [S10]. The second error process takes place when the pulse duration of the excitation laser $T_{\text{pulse}}$ approaches the excited state lifetime $1/\Gamma$. In such a case, the QD could be driven twice emitting multiple photons within the excitation pulse.

To investigate the entanglement fidelity under these errors, for a single optical excitation in the Monte Carlo simulation, we first estimate the probabilities of off-resonant excitation (i.e., probability of driving $|\uparrow\rangle \to |\Downarrow\downarrow\uparrow\rangle$) and two-photon emission, which are found by solving optical Bloch equations describing the excitation and emission from a two-level system:

$$\begin{cases} \dot{\rho}_{gg0} = \Omega(t) \cdot \text{Im}(\rho_{eg0}) \\ \dot{\rho}_{ee0} = -\Omega(t) \cdot \text{Im}(\rho_{eg0}) - \rho_{ee0}\Gamma \\ \dot{\rho}_{eg0} = i \cdot \Delta_L \cdot \rho_{eg0} + i \cdot \frac{\Omega(t)}{2} \cdot (\rho_{ee0} - \rho_{gg0}) - \rho_{eg0}\frac{\Gamma}{2} \end{cases} \tag{16}$$

$$\begin{cases} \dot{\rho}_{gg1} = \Omega(t) \cdot \text{Im}(\rho_{eg1}) + \rho_{ee0}\Gamma \\ \dot{\rho}_{ee1} = -\Omega(t) \cdot \text{Im}(\rho_{eg1}) - \rho_{ee1}\Gamma \\ \dot{\rho}_{eg1} = i \cdot \Delta_L \cdot \rho_{eg1} + i \cdot \frac{\Omega(t)}{2} \cdot (\rho_{ee1} - \rho_{gg1}) - \rho_{eg1}\frac{\Gamma}{2} \end{cases} \tag{17}$$

$$\dot{\rho}_{gg2} = \rho_{ee1}\Gamma, \tag{18}$$

where $\rho_{ijk}$ is the atomic density matrix element $|i\rangle\langle j|$, $i,j \in \{e,g\}$ and $k$ is the number of emitted photons considered up to 2 photons, i.e., $\rho_{gg0}$ ($\rho_{ee0}$) is the ground-state (excited-state) population in which no photon is emitted. $\Omega(t)$ is the time-dependent optical Rabi frequency, assuming a Gaussian profile for the excitation laser. $\Delta_L$ is the laser detuning relative to an optical transition. $\Gamma$ is the excited-state decay rate assumed to be equal for $|\Uparrow\downarrow\uparrow\rangle$ and $|\Downarrow\downarrow\uparrow\rangle$.

To model the current experiment, we set the laser detuning $\Delta_L = 12\,\text{GHz}$ from the undesired transition $|\uparrow\rangle \to |\Downarrow\downarrow\uparrow\rangle$ to estimate the probability of off-resonant excitation, and $\Delta_L = 2\,\text{GHz}$ from the desired transition $|\downarrow\rangle \leftrightarrow |\Uparrow\downarrow\uparrow\rangle$ for computing the re-excitation probability. For the optimized InAs and GaAs QDs simulations, the corresponding $\Delta_L$ can be found in Supplementary table. 2. For simulations with a Gaussian excitation pulse, Eqs. (16)-(18) can only be solved numerically. Therefore, to verify our simulation code we now choose a square pulse and consider only the off-resonant excitation error, which enables a direct comparison with the closed form derived analytically in Ref. [S10]:

$$\mathcal{F}_{\text{GHZ}}^{(N)} = \frac{1}{2} \frac{D_1^N + D_2^N}{(D_2 + D_3)^N}, \tag{19}$$

where the relevant terms read

$$D_1 = |c_0 c_2|^2$$
$$D_2 = |c_0 c_2|^2 + |c_0 \phi_2|^2 + |\phi_0 c_2|^2 + |\phi_0 \phi_2|^2$$
$$D_3 = |c_1 c_3|^2 + |c_3 \phi_1|^2 + |c_1 \phi_3|^2 + |\phi_3 \phi_1|^2 + |c_3 c_2|^2 + |c_3 \phi_2|^2 + |\phi_3 c_2|^2 + |\phi_3 \phi_2|^2,$$

with the wavefunction coefficients

$$|\phi_1|^2 = \frac{3\sqrt{3}\pi}{8\tilde{\Delta}} - \frac{3\pi^2}{2\tilde{\Delta}^2}\left(\frac{3}{8} - \frac{1}{\pi^2}\right), \ |\phi_2|^2 = \frac{\pi\sqrt{3}}{8\tilde{\Delta}}|c_2|^2, \ |\phi_3|^2 = \frac{3}{16}\left(\frac{\sqrt{3}\pi}{8\tilde{\Delta}} - \frac{3\pi^2}{16\tilde{\Delta}^2}\right), |\phi_0|^2 = \frac{13\sqrt{3}\pi}{128\tilde{\Delta}}|c_2|^2$$

$$|c_0|^2 = 1, \ |c_1|^2 = \frac{\sqrt{3}\pi}{2\tilde{\Delta}}, \ |c_2|^2 = 1 - |c_1|^2, \ \tilde{\Delta} = \frac{\Delta_L}{\Gamma}.$$

The expressions above assume perfect frequency filters and a square pulse of the optimal duration $T_{\text{pulse}}^{\text{opt}} = \sqrt{3}\pi/\Delta_L$ such that a optical $\pi$-pulse resonantly drives the transition $|\downarrow\rangle \leftrightarrow |\Uparrow\downarrow\uparrow\rangle$, while a $2\pi$-pulse is applied on the off-resonant transition. We reproduce this condition in our simulation and compare it to the analytical form in Eq. (19), see Supplementary Fig. 15(a). We observe very good agreement between theory and simulation over a laser detuning from $\Delta_L = 10\,\text{GHz}$ to $100\,\text{GHz}$. Supplementary Fig. 15(b) shows the predicted scaling of the off-resonant excitation error with photon numbers.
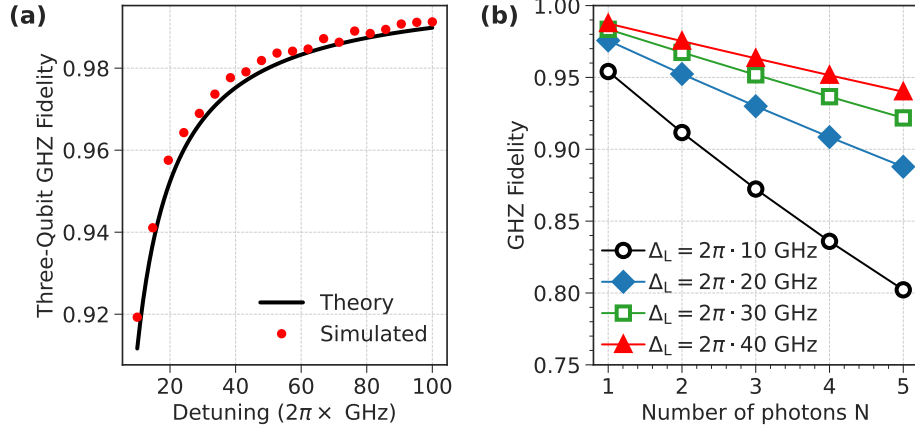
**Supplementary Figure** 15. (a) Comparison between the simulated and analytical fidelities under off-resonant excitation error. (b) Plot of $\mathcal{F}_{\text{GHZ}}^{(N)}$ as a function of photon number $N$ for different values of the laser detuning $\Delta_L$.

## X.  PHOTON DETECTION EFFICIENCY

| Loss source | Efficiency % | Loss (dB) | Source |
|---|---|---|---|
| Waveguide-coupling factor $\beta$ | 90 | -0.46 | Estimated |
| Less-than-$\pi$ excitation pulse | 80 | -0.97 | Estimated |
| Emission into the zero phonon line | 95 | -0.22 | Ref. [S3] |
| Two-sided waveguide configuration | 50 | -3.01 | Estimated |
| Propagation loss in GaAs waveguide (free carrier absorption, grating coupler loss) | 56 | -2.52 | Measured |
| Transmission in the collection fiber | 60 | -2.22 | Measured |
| **Total efficiency from quantum dot to the collection fiber** | **11.5** | **-9.4** | |
| | | | |
| 50/50 Beamsplitter in TBI | 50 | -3.01 | Estimated |
| Additional loss in TBI due to other optic elements | 60 | -2.22 | Measured |
| Total transmission after two etalon filters | 90 | -0.46 | Measured |
| Fiber coupling to the detection fiber before SNSPDs | 70 | -1.55 | Measured |
| Fiber transmission to SNSPDs | 85 | -0.71 | Measured |
| SNSPDs detection efficiency | 70 | -1.55 | Measured |
| **State characterization and detection** | **11.2** | **-9.5** | |
| **Total loss from quantum dot to detection** | **1.3** | **-18.9** | |

**Supplementary Table** 4.  Compilation of all photon loss sources in the entanglement experiment.  SNSPDs stands for superconducting nanowire single-photon detectors from PhotonSpot.

[S1] M. C. Löbl, S. Scholz, I. Söllner, J. Ritzmann, T. Denneulin, A. Kovács, B. E. Kardynał, A. D. Wieck, A. Ludwig, and R. J. Warburton, Communications Physics **2**, 93 (2019).

[S2] D. A. B. Miller, D. S. Chemla, T. C. Damen, A. C. Gossard, W. Wiegmann, T. H. Wood, and C. A. Burrus, Phys. Rev. Lett. **53**, 2173 (1984).

[S3] R. Uppu, F. T. Pedersen, Y. Wang, C. T. Olesen, C. Papon, X. Zhou, L. Midolo, S. Scholz, A. D. Wieck, A. Ludwig, and P. Lodahl, Science Advances **6**, eabc8268 (2020).

[S4] L. Midolo, T. Pregnolato, G. Kiršanskė, and S. Stobbe, Nanotechnology **26**, 484002 (2015).

[S5] M. H. Appel, A. Tiranov, S. Pabst, M. L. Chan, C. Starup, Y. Wang, L. Midolo, K. Tiurev, S. Scholz, A. D. Wieck, A. Ludwig, A. S. Sørensen, and P. Lodahl, Phys. Rev. Lett. **128**, 233602 (2022).

[S6] D. A. Gangloff, G. Éthier Majcher, C. Lang, E. V. Denning, J. H. Bodey, D. M. Jackson, E. Clarke, M. Hugues, C. Le Gall, and M. Atatüre, Science **364**, 62 (2019).

[S7] M. H. Appel, A. Tiranov, A. Javadi, M. C. Löbl, Y. Wang, S. Scholz, A. D. Wieck, A. Ludwig, R. J. Warburton, and P. Lodahl, Phys. Rev. Lett. **126**, 013602 (2021).

[S8] P. Tighineanu, C. L. Dreeßen, C. Flindt, P. Lodahl, and A. S. Sørensen, Phys. Rev. Lett. **120**, 257401 (2018).

[S9] R. Stockill, C. Le Gall, C. Matthiesen, L. Huthmacher, E. Clarke, M. Hugues, and M. Atatüre, Nat Commun **7**, 12745 (2016).

[S10] K. Tiurev, P. L. Mirambell, M. B. Lauritzen, M. H. Appel, A. Tiranov, P. Lodahl, and A. S. Sørensen, Phys. Rev. A **104**, 052604 (2021).

[S11] M. L. Chan, A. Tiranov, M. H. Appel, Y. Wang, L. Midolo, S. Scholz, A. D. Wieck, A. Ludwig, A. S. Sørensen, and P. Lodahl, npj Quantum Information **9**, 49 (2023).

[S12] P. Lochner, J. Kerski, A. Kurzmann, A. D. Wieck, A. Ludwig, M. Geller, and A. Lorke, Phys. Rev. B **103**, 075426 (2021).

[S13] L. Besombes, K. Kheng, L. Marsal, and H. Mariette, Phys. Rev. B **63**, 155307 (2001).

[S14] B. Krummheuer, V. M. Axt, and T. Kuhn, Phys. Rev. B **65**, 195313 (2002).

[S15] E. A. Muljarov and R. Zimmermann, Phys. Rev. Lett. **93**, 237401 (2004).